Supplementary Information (SI) for Journal of Materials Chemistry A.

Constructing Dual Silsesquioxane-Crosslinked Network Channels in Hybrid Polymer Membranes for Dendrite-Free and Durable High-Power LMBs

Lingli Liu [b,c]+*, Xuefeng Gui [a,d,e]+, Dongxia Li [a, b, f]+, Qiong Lin [a,b], Tian Zhang [a,d], Longfeng Sun [a,b], Zhongxin Wang [a, b, e], Xuan Song, [a,b] Xiangfeng Sun [a, b, d], Yuxin Xue [a, b, e], Chongxian Luo [a, b, f], Kai Xu [a, b]* .

[a] Guangdong Provincial Key Laboratory of Organic Polymer Materials for Electronics, Guangzhou Institute of Chemistry, Chinese Academy of Sciences, P. O. BOX 1122, Guangzhou 510650, People's Republic of China.

[b] University of Chinese Academy of Sciences, Beijing 100049, People's Republic of China.

[c] Zhuhai Titan Ink new material Co.,Ltd, Titan Inkjet Union Ltd. No. 388, Yongnan Road, Xiangzhou District, Zhuhai 519000, People's Republic of China.

[d] *CAS Engineering Laboratory for Special Fine Chemicals, Guangzhou 510650, China*

[e] *CASH GCC Shaoguan Research Institute of Advanced Materials, Shaoguan 512000, China*

[f] *CASH GCC (Nanxiong) Research Institute of Advanced Materials Co, Ltd, Nanxiong 512000, China*

\+ These authors contributed equally to this work.

* Correspondence to Lingli Liu, University of Chinese Academy of Sciences, Beijing 100049, People's Republic of China.
Email: liulingli16@mails.ucas.ac.cn.

* Correspondence to Kai Xu, Guangzhou Institute of Chemistry, Chinese Academy of Sciences, P. O. BOX 1122, Guangzhou 510650, People's Republic of China.
Email: xk@gic.ac.cn; Fax: +86 20 85231058; Tel: +86 20 85232302.

Contents

Experimental methods......1

Materials:......1

Preparation of cage-like deca(methacryloxypropyl) silsesquioxane (DMSQ) 2

Preparation of the cage-like octakis(aminophenyl) silsesquioxane (OAPS) 3

Preparation of Functional Hybrid Membranes......3

Chemical Characterization:......5

Supporting Notes(1-5) 9

Supporting Figures and Tables (S1-S15, Table S1-S6) 19

Supporting References 37

Experimental methods

Materials

Poly (vinylidene fluoride hexafluoropropylene) (PVDF(hfp) 2800-00, the proportion of 1.77~1.80 g cm^{-3}), Poly (methyl methacrylate) (PMMA-DR101, the proportion of 1.15 g cm^{-3}) were purchased from Arkema (Serquigny, France). Benzophenone (BP), Ammonium ceric nitrate (ACN), N-N-Dimethylacetamide (DMAc), acetone (ACE), Ethyl Alcohol (Et-OH), N-methyl pyrrolidone (NMP) and dichloromethane (DCM) were purchased from Aladdin Chemical Reagent Co., Ltd (Shanghai, China). The electrospinning device was purchased from Foshan lepton precision measurement and control technology co., Ltd. Polypropylene (PP) syringes with a 10 mL volume, stainless-steel needles of 21G (inner diameter, 0.51 mm; outer diameter, 0.81 mm) and 25 G (inner diameter, 0.26 mm; outer diameter, 0.51 mm) were purchased from Shenzhen Contriu Technology Co.,Ltd. Functional monomers deca(methacryloxypropyl) silsesquioxane(DMSQ-T10, Mn=1790g/mol) and octa(aminophenyl) sesquisiloxane (OAPS, Mn=1152g/mol) were synthesized in laboratory. The commercial separator used in the control case (Celgard 2500, thickness: 25 um, porosity 50%) was supplied by Celgard LLC. The electrolyte for symmetric Li/Li and full LFP/Li cells consiste of ethylene carbonate (EC)/ diethyl carbonate (DEC)/ ethyl methyl carbonate (EMC) (1/1/1, by volume) with 1 M $LiPF_6$, while asymmetric Li/Cu cells consists of mixed solvent of 1,3-dioxolane (DOL) and 1,2-dimethoxyethane (DME) (1/1, by volume) with 1 M lithium bis-(trifluoromethanesulfonyl) imide (LiTFSI) and 1 wt% $LiNO_3$. Aluminum foil (thickness of 10 um), Li metal foil (two thickness specifications utilized in this research: 450 and100 um), Cu foil (thickness of 9 um) and electrolyte were bought from Canrd Corporation.

Preparation of cage-like deca(methacryloxypropyl) silsesquioxane (DMSQ)

DMSQ was synthesized via a method described in our previous work [1]. Into a 250 mL three-necked round-bottom flask, 100 mL of isopropanol and 50 g of (3-methacryloxypropyl)-trimethoxysilane were introduced, while 2.14 g of tetramethylammonium hydroxide was dissolved in 9.8 mL of distilled water and added dropwise into this solution. This mixture was stirred at 50 °C for 8 h, and then the solvent was removed via rotary evaporation. Subsequently, 100 mL of toluene was added to the hydrolysis products in a 250 mL three-necked flask that was equipped with a water segregator and a condenser, and 2.38 g of tetramethylammonium hydroxide that had been pre-dissolved in 6.9 mL of distilled water was added dropwise under nitrogen atmosphere. The mixture was refluxed for 10 h until no water was distilled out. A colorless viscous liquid was obtained after washing, and fully evaporating the solvent. DMSQ was precipitated and separated from the mixed product via treatment with methanol and purified by recrystallization in acetone, while the remaining viscous liquid was isolated via silica gel column chromatography in a solvent mixture.

FTIR (KBr): 1716 (s; C=O), 1637 (m; C=C), 1116 (s; Si–O–Si); ^{29}**Si-NMR** (δ, ppm): DMSQ: -68.1; ^{1}**H-NMR** (DMSO-d_6): $SiO_{1.5}CH_2$ (a) CH_2 (b) CH_2 (c) CO_2CCH_3 (d) CH_2 (e and f), a:0.68 ppm, 2H; b: 1.74 ppm, 2H; c: 4.09 ppm, 2H; d: 1.92 ppm, 3H;e and f: 5.54 ppm, 1H and 6.08 ppm, 1H. **MALDI-TOF MS** (complex with Na^+): DMSQ: 1814 Da.

Preparation of the cage-like octakis(aminophenyl) silsesquioxane (OAPS)

OAPS was synthesized by following Laine and co-workers' method with modifications, which was derived from octakis(phenyl) silsesquioxane through nitration and reduction. The used octakis-(phenyl) silsesquioxane was prepared by following Brown and co-workers' method [2].

FTIR (KBr): 3365 (w; N–H), 1116 (s; Si–O–Si); **^{29}Si NMR** (d, ppm): -70.5, -79.2; **^{1}H NMR** (DMSO-d6) (δ, ppm) 6.0–7.8 (b, 2.0H), 5.0–5.4 (b, 1.0H); **GPC**: Mn =1146, Mw=1335, Mw/Mn=1.16

Preparation of Functional Hybrid Membranes

PVDF(HFP) and PMMA (3:1, *m*/*m*) were dissolved inmixed solvent of DMAc and acetone (2:3, *V*/*V*) with concentrations of 18 *wt.*%, and vigorously stirred at room temperature for 6 h to obtain the homogeneous electrospinning precursor solution. Subsequently, the homogeneous electrospinning solution was loaded into a 10 mL syringe fitted with a 21G for the following electrospinning process. The content of each components in electrospinning mixture is as follows: functional monomer silsesquioxanes containing 10 *wt.*% DMSQ and different additions (5 *wt.*% or 10 *wt.*%) of OAPS (relative to the PVDF(HFP)/PMMA polymer matrix); 5 *wt.*% of photo-initiator BP (relative to DMSQ) and 5 *wt.*% ACN (relative to the total of two functional monomers); DMAc/ethanol (1:4, *V*/*V*) as the solvent. Various mass concentration of two CSQ monomer solution were prepared after fully mixed at room temperature for 6 h to get a homogeneous solution. The preparation of each functional monomer solution was made up of either DMSQ+BP or OAPS+ACN dissolved in 2.5 ml component solvent with different additions. The functional monomer solution was poured into a 5 mL syringe with a 25G needle placed on an infusion syringe pump (model KDS100) to regulate the monomer solution efflux velocity.

Functional hybrid membranes (FHMs) were prepared via a rational synthetic route, which involved a combination of concurrent electrospinning/electrospraying strategies and UV-initiated *in-situ* grafting polymerization, where the blending solution containing Poly(vinylidene fluoride hexafluoropropylene) PVDF(HFP) and Poly(methyl methacrylate) PMMA were electrospun to construct a porous flexible network membrane. Meanwhile, DMSQ and OAPS were respectively adopted as photoinitiated *in-situ* grafting monomers and crosslinking agents and were simultaneously electrosprayed onto the surface of electrospun fibers to fabricate the functional hybrid membranes under ultraviolet irradiation throughout the preparation process. During this process, C–H bonds are activated and then undergo hydrogen-abstracting reactions with the polymer substrate under UV irradiation, which consequently generates surface radicals on the fibers. Methacrylate groups on DMSQ monomer are linked with surface radicals due to photochemical grafting polymerization on the membrane, while the phenylamino groups on OAPS monomers are subsequently crosslinked with residual methacrylate groups via aza-Michael crosslinking reaction. In the electrospinning process, a homogeneously blended solution containing the DMSQ monomers and polymer precursors was extruded from a syringe to form a Taylor cone and then ejected onto rotating collector to thus generate a porous fiber network with uniform film thickness, when a high voltage was supplied between needle and the aluminum roller. Concurrently, another paratactic syringe contained a OAPS monomers solution which was electrosprayed onto the fiber film. Following the electrospraying/electrospinning treatment the prepared membranes were irradiated with ultraviolet light (generated by 70°C mercury vapor lamp) for 1h to ensure that the involved chemical reactions had reached completion. Subsequently, the membranes were ultrasonically cleaned with anhydrous ethanol three times to remove the excess unreacted monomer and other impurities and then dried in a blast oven at 70 °C for over 18 h. According to hybrid addition by functional DMSQ and OAPS monomers, we named membranes for pristine membrane (PM) with no modification and FHM-D with solely grafted DMSQ, respectively, while the FHM-D/A5 and FHM-D/A10 modified by two monomers but different additions (5 *wt.*% or 10 *wt.*%) of OAPS.

Chemical Characterization:

The membranes were characterized by Fourier transform infrared (FT-IR) spectra using a Bruker Tensor 27 infrared spectrophotogram KBr discs. Differential scanning calorimeter (DSC) was performed on a Perkin-Elmer Diamond DSC with a heating rate of 10 ^{o}C /min under nitrogen flow (20 ml/min). Thermogravimetric analysis (TGA) was performed on a NETZSCH TG 209 F3Tarsus thermogravimetric analyzer with a heating rate of 10 ^{o}C /min under a nitrogen flow in the temperature range of 40~700 ^{o}C to determine the thermal degradation of different compositions of the membranes. Element analysis was recorded on a Bruker 400 Energy dispersive spectrometer. Morphologies of the membranes were investigated by scanning electron microscope (SEM) using a Hitachi S-4800 instrument (Hitachi High-Technologies Co., Japan) with a low acceleration voltage of 1.0 kV. The microscopic morphologies and EDS mapping of lithium foils and membranes were performed by using TESCAN Brno, s.r.o. MIRA3 LMH field-emission scanning electron microscopy (FT-SEM) with an Oxford Instruments NanoAnalysis INCA Energy 150 X-ACT energy dispersive spectrometer (EDS). The tensile strength and puncture strength of membranes were measured by an electronic universal-testing machine (H10KS, HOUNSFIED Co., UK), with the reference to the test standard of GB/T 1040 and GB/T 10004 respectively. X-ray photoelectron spectroscopy (XPS) analysis was analyzed by a Thermo Fisher ESCALAB 250XiT instrument with Mg Kα radiation (1253.6 eV) at a scan step of 0.1 eV. Impedance versus frequency and Ionic conductivity of those electrochemical properties were performed by Autolab electrochemical workstation (PGSTAT 302N, Metrohm, Switzerland) and battery test equipment (LAND-2001A, Land Electronic, China). The mechanical properties of membranes were researched by dynamic mechanical analysis (DMA) using a DMA1 apparatus (METTLER TOLED, Switzerland).

Assembly and electrochemical characterization of Li metal batteries

All cells assembled by CR2032 type coin cell under in an argon-filled glove box. The electrochemical performance of the cells was measured at room temperature by using a LAND batteries tester. Symmetric Li|Li cells were prepared with two Li metal foils (thickness of 450 um, diameter of 15.6 mm) as the electrode and celgard 2500, Pristine Membrane or the FHMs as separator (diameter of 19 mm). The liquid electrolyte was composed of 1.0 $_{M}$ $LiPF_6$ dissolved in EC/ DEC/ EMC (1:1:1, by volume) and the dosage of electrolyte was limited to 70 μl via micropipette gun.

The asymmetric Li|Cu cells were fabricated as Li foil (thickness of 100um, diameter of 15.6 mm) as the anode, polished copper (thickness of 9 um, diameter of 12 mm) as the cathode, and prepared membranes as the separator. Lean 60 μl electrolyte of 1.0 $_{M}$ LiTFSI dissolved in DOL/DME (1:1, by volume) with 1 *wt*% $LiNO_3$ additive was used in assembling the coin cells. Additionally, the galvanostatic charge-discharge method was carried out on Li|Cu cells testing. Li was first deposited onto copper foil at different current densities with fixed capacity densities and then stripped to 1.0 V at the corresponding current density.

The LFP electrodes were produced by a slurry–coating method. The cathode slurry was prepared by mixing 80 *wt*% $LiFePO_4$ cathode active material, 10 *wt*% Super P as a conductive agent, and 10 *wt*% PVDF as binder dissolved in NMP. This homogenous slurry was coated onto an aluminum foil (thickness of 10 um) after mixing thoroughly for 6 h and then dried at 110 ^{o}C under vacuum for 12 h. Additionally, the thickness of the cathode is 100 um, and the diameter is punched in 12 mm. The areal loading of $LiFePO_4$ cathode is about 3.2 mg cm^{-2} and the specific capacity of commercial $LiFePO_4$ is near 150 mAh g^{-1}. The LFP|Li cells were fabricated by using $LiFePO_4$ as the cathode, polished Li foil (thickness of 100um, diameter of 15.6 mm) as the anode, and PP or prepared FHMs as the separator. The electrolyte was the same with symmetric cells, but the dosage of electrolyte was fixed at 50 μl.

The average CE is calculated by dividing the total stripping capacity by the total deposition capacity after the formation cycle. For the Aurbach CE test, a standard protocol was followed: (1) perform one initial formation cycle with Li deposition of 1 mAh/cm^2 on Cu under 0.5 mA/cm^2 current density and stripping to 1 V; (2) deposit 1 mAh/cm^2 Li on Cu under 0.5 mA/cm^2 as a Li reservoir; (3) repeatedly strip/deposit Li of 1 mAh/cm^2 under 0.5 mA/cm^2 for 10 cycles; (4) strip all Li by charging the cell to 1 V. The LFP coin cells were cycled between 2.7 and 4.0 V, after the first two activation cycles at 0.2C charge/discharge, the cells were cycled at different rates. All cells were cycled under ambient conditions without temperature control (1 C = 170 mA/g).

Porosity and Electrolyte Uptake

The separator porosity was determined by immersing the membrane in n-butanol for 1 h. The porosity(P) of the membrane was calculated using the following equation:

$$P\% = \frac{M_2 - M_1}{\rho_b \cdot V_m} \times 100\% \quad (1)$$

where M_1 and M_2 denote the mass of dry membranes and after fully saturated with *n*-butanol, respectively, ρ_b is the densities of *n*-butanol, V_m represents the volume of the membranes (calculated by multiplying the surface area and thickness of the membranes).

The electrolyte uptake (η) was calculated by the weight of separator before (W_o) and after (W) soaking in the liquid electrolyte under vacuum for 1h as:

$$\eta = \frac{W - W_o}{W_o} \times 100\% \quad (2)$$

The excess n-butanol or electrolyte solution on the separator surfaces is absorbed with a dried filter paper before measuring the weight.

Ionic conductivity and lithium-ion transference number measurement

The ionic conductivities of PP and FHMs separator were calculated based on the following equation:

$$\sigma = \frac{L}{R_b \cdot A} \times 100\% \quad (3)$$

where σ is the ionic conductivity, Rb is the bulk resistance from the EIS test, and L and A are the thickness and area of the separator, respectively.

The lithium-ion transference number (t_{Li^+})was measured using the method described by equation (4) of Abraham et al[3]. Symmetric Li|Li cell was assembled with different separators and then the polarization currents (including the initial (I^{o}) and steady-state (I^{ss}) current values) were recorded under a low polarization potential (ΔV) of 10 mV. The initial and steady-state values of the bulk resistances (R_b^{o} and R_b^{ss}) and electrode|electrolyte interfacial resistances (R_i^{o} and R_i^{ss}) were examined before and after the potentiostatic polarization via EISs. The $t_{Li}{}^{+}$ was calculated based on the following equation:

$$t_{Li}^{+} = \frac{I^{ss}R_b^{ss}\,(\Delta V - I^{o}R_i^{o})}{I^{o}R_b^{o}\,(\Delta V - I^{ss}R_i^{ss})} \tag{4}$$

The method of the NLDFT (Non-local Density Functional Theory)

The NLDFT (Non-local Density Functional Theory) method is widely used for measuring micro- and mesopore distributions due to its ability to provide a unified analysis across the entire pore size range. For micro-mesoporous composites, NLDFT offers a more comprehensive analysis compared to traditional methods like BJH or HK, as it accounts for both micro- and mesopore contributions through a single theoretical framework. When applying NLDFT, it is crucial to select appropriate adsorbents (e.g., nitrogen or argon) and consider the material's surface characteristics. For this work, NLDFT can be used with nitrogen adsorption at 77 K for mesoporous materials like MCM-41. Additionally, NLDFT models are available in commercial software (e.g., Anton Paar’s QSDFT), which further enhance the accuracy of pore size distribution analysis by incorporating surface roughness and anisotropy corrections.

The test of DFT calculation

The molecular geometries of isolated D/A-CSQs and their Li^+ complexes were systematically optimized through a multistage computational protocol. Initial structural exploration employed the semi-empirical GFN-xTB method[4, 5], where the Molclus program generated one hundred candidate adsorption configurations for each complex. These configurations underwent preliminary geometry optimization using the xTB package, with the lowest-energy structure selected for subsequent refinement. DFT calculations were then performed using the PBE0 functional[6] combined with the def2SVP basis set[7]. All calculation were performed using the Gaussian 16 package and dispersion corrections using DFT-D3 method. Basis set superposition error (BSSE) corrections were rigorously applied through the counterpoise method. Frontier molecular orbital distributions were visualized using the Visual Molecular Dynamics (VMD) platform, with isosurface thresholds standardized at ± 0.02 e/$Å^3$.

The absorption energy (E_{Abs}) formula is calculated as follows:

$$E_{Abs} = E_{total} - E_{sub} - 10 * E_{Li} \qquad (5)$$

where E_{total} is the total energies of the optimized complex structures; E_{sub} is the energy of substrate; E_{Li} is the energy of Li atom.

Supporting Notes

Supporting Note 1. The Electrospinning/electrospraying Process and Chemical Characterization the FHMs

The current experimental setup requires further optimization for scalable and cost-effective production. Based on the current advancements in electrospinning technology, we can replace the traditional single-nozzle counterpart with multinozzle electrospinning, as it enables enables the simultaneously generation of multiple jets, thereby yielding more materials. Besides multinozzle electrospinning, needleless electrospinning and bubble electrospinning are two other available selections which can enable many Taylor cones to form a large number of jets at the same time. These developed electrospinning techniques show great capability for mass production of electrospun materials. Furthermore, the synthetic costs of materials can be significantly reduced by recycling organic solvents through the condensation technology[8]. In addition, Ramakrishna[9] et al. described electrospinning methods and process parameters at laboratory and industrial scales, that had been put into use with emerging equipment. Some electrospun products have already been commerialized and used in energy storage application such as separators (e.g., Jiangxi Advanced Nanofiber S&T Co., Ltd). Therefore, with the continuous development of spinning technology while we continue to optimise the preparation conditions, we expect to be able to meet the requirements for commercial production in the future.

The thermal stability of the separators has a key influence on the performance of LMBs, and the typical DSC profiles of pristine membrane(PM) and the FHMs obtained via three heating-cooling-heating sequences are presented in **Figure S1c**. Compared to the pristine PVDF(HFP)/PMMA membrane, the exothermic peak exhibited by the FHMs during the second heating-cooling process had shifted towards a high temperature and the endothermic enthalpy was increased, thus indicating that the thermal stability of the FHMs were enhanced. None of the FHMs exhibited any amorphous crystalline phase transition peaks during the cooling process, and the lack of such peaks can be attributed to the generation if a highly microporous inner structure during the crystallization process that enabled rapid ion transport through the membrane, more details are summarized in **Table S1**. In order to further investigate the thermal stability of the hybrid membranes, membranes were characterized via thermogravimetric analysis (TGA) and the results are clearly depicted in **Figure S1d**. The FHM samples showed higher initial decomposition temperatures and residual masses at an elevated temperature (600°C) compared with PM, and generally increased with an increasing CSQs content, thus confirming the successful introduction of highly thermally stable CSQ monomers and demonstrating that the formed crosslinked structure provided the membranes with thermal stabilities. In addition, the calculated grafting ratio of functional monomers was over 80% on the basis of the control reaction. Therefore, based on the improved thermal stability as well as the high grafting ratio exhibited by the FHMs, we can confirm that the chemical reactions readily proceeded between the polymer fibers and functional monomers and that the CSQs were successfully introduced into the nanofiber matrices.

Supporting Note 2. Mesoporosity Characterization of the FHMs

N_2 adsorption/desorption tests were performed to evaluate the nanoscale porosity of the prepared membranes with and without DMSQ and OAPS monomers. All membranes gave rise to type IV nitrogen sorption isotherms (**Figure 2a**), and the FHM-D/A10 exhibited noticeable hysteresis at a medium pressure range, which is consistent with a membrane containing numerous mesopores, whereas indistinct hysteresis was noted for other FHMs and the PM had much lower porosity in the measured region than that of the FHMs. The Brunauer–Emmett–Teller (BET) surface areas calculated from the isotherms in the range from 0.02 to 0.2 of relative pressures (*P*/*P*0) and measured pore volumes are summarized in **Table S2**. As expected, the fibers of fabricated membranes were near nanoscale diameter and the subtle hole structure derived from hybrid nanoparticles CSQ monomers also resulted in very little microporosity (< 2 nm) but more mesoporosity (2-50 nm) for membranes as characterized by NLDFT calculations. Note that the newly formed micropores with diameters in the ranges of 23-38 and 40-50 nm could be detected in the FHMs via N_2 sorption measurements. Indeed, as the membrane modification degree increased, an enlargement of the surface areas and pore volumes of the mesopores was observed. It can be seen that the cumulative volume of the FHMs increased rapidly when the pore diameters were in the range of 2-30 nm and had a second rise near 50 nm. As exhibited in **Figure 2a-c**, the PM increased over the pore diameter range of 10-60 nm, indicated that the pore diameters of the as-prepared membranes were mainly situated in the mesopore range (2-50 nm).

Supporting Note 3. Basic electrochemical performance of the as-prepared membranes

To investigate how the grafted and cross-linked CSQ monomers influence the kinetics of the electrochemical process, various electrochemical experiments were performed using Li|Li symmetric cells with the above separators. The Nyquist plots of cells with different separators, as compared in **Figure 2f**. The *x*-intercept in the ultrahigh-frequency range was attributable to bulk resistance (R_b), which can be used to evaluate the ionic conductivity of a cell[10]. Meanwhile, the semicircle diameter at the high-frequency range was assigned to the interfacial resistance (R_i) of the interfacial charge transfer phenomena between the Li anode and the electrolyte.[11] Basically, the room temperature ionic conductivity of each separator was calculated based on the EIS data and shown in the inset of **Figure 2f**, where it can be seen that the values of the FHMs were much higher than those of the PP separator and PM. Significantly, the impedance R_i in the initial state was much smaller for electrospun membrane-based cells compared with that equipped with a PP separator due to the characteristic porosity and polymer chemical affinity for electrolyte. As expected, the R_i values of the FHMs continued to decrease as the grafting and crosslinking degrees increased, signifying the good interface compatibility formation in cells. Moreover, the Li-ion transference number (t_{Li}^+) is another vital parameter for the interface between electrolyte and membrane systems because a high t_{Li}^+ is expected to reduce the Li-ion concentration polarization, suppress the growth of lithium dendrites, and enhance the electrochemical performance of LMBs.[12] As shown in **Figure 2g-h**, the cell equipped with the FHM-D/A10 exhibits a high t_{Li}^+ value of 0.93, which is notably higher than that of the PM (0.457), commercial PP separator (0.21), and other polymer electrolytes.[13-14] Besides, the t_{Li}^+ values of cells with other FHMs are also much higher than that of the control separators. The increased t_{Li}^+ of the FHMs can be attributed to the highly mesoporous structure of these membranes to provide accessional Li^+ transport pathways, as well as the presence of grafted high-affinity chains for electrolyte to decrease charge transfer resistance. On the other hand, the presence of numerous amide/amine groups throughout the FHMs could effectively facilitate uniform distribution and fast transport of Li-ions, and thus the t_{Li}^+ measurements are consistent with previously reported ionic conductivity and EIS data.[15]

Supporting Note 4. Mechanism Study on XPS analysis

The narrow scan XPS spectra, including deconvoluted specific peaks of various elements such as C1s, O1s, F1s, Li1s, and N1s, of SEI on the side facing the Li anode (**Figure 5a**) and facing the membrane (**Figure 5b**) are shown, along with the oxidation states of the elements, relevant peak assignments, and corresponding element concentrations, respectively (**Figure S8 a,b**). In the C1s spectra of the SEI layer, the main peaks located at 284.4, 286.5, 289.5, and 290.7 eV are ascribed to C–C/C–H, $ROCO_2Li$, Li_2CO_3, and C–F bonds, respectively.[16-17] Among these species, the source of the fluorine-containing C–F groups can be attributed to the PVDF(HFP), while the remaining species primarily originate from the reduction products of the organic electrolyte. Meanwhile, the components of the SEI observed in the F1s spectra include LiF, $LiPF_6$, and C–F, which exhibit signals at 685.2, 687.1, and 688.2eV, respectively. The LiF observed in the F1s spectra may stem from the decompositions of PVDF(HFP) and $LiPF_6$. According to Li1s and O1s spectra, an Li_2O (53.9 and 529.1eV, respectively) species was also present in the SEI products, and thus the detected SEI components were consistent with results reported in the previous literature.[18] Besides, the peak at 532.8 eV corresponding to Si–O bonds observed in the O1s spectrum, the signal representing C–N bonds (286.2 and 397.8 eV) observed respectively in the C1s spectrum and N1s spectrum provided further confirmation that the FHMs had been successfully prepared and that their surfaces were endowed with numerous functional groups, as shown in **Figure 5a, b**. On the other hand, groups in the nano-sheets comprising the FHMs have a strong affinity towards the Li anode, because those components in the SEI layer are likely derived from the functional CSQ nanocages in

FHMs. A weak signal corresponding to inactive metallic Li^o (53 eV) was present in the Li1s spectrum in the Li anode-facing side SEI of control and FHM-D, which predicted the existence of irregular Li deposits or inactive Li in the SEI layer. In contrast, no inactive Li species were observed in the XPS spectra of FHM-D/A5 (**Figure S8c**) and FHM-D/A10 (**Figure 5a**), indicating that a higher OAPS content enhances the protection of the Li metal surface. Notably, both sides of the interface layer contain the same components and relevant element peak assignments, which demonstrated that the FHMs acted as an active substance to participate in SEI layer formation. Therefore, XPS spectra provide conclusive evidence of a strong chemical affinity between the FHMs within the electrolyte and the Li metal anode, providing further evidence that the nanosheets in the FHMs can be considered as *in-situ* active sites enabling the formation of the SEI layer. Further analysis of the Li anode-facing side of the SEI layer, compared with the control sample, revealed that strongly enhanced peaks corresponding to the $ROCO_2Li$ moieties from the FHM-D and FHM-D/A10 are also observed in the XPS spectra of the anode-facing side of the corresponding SEI layers. In particular, these peaks were observed at 286.5 eV in the C1s spectrum, 57.4 eV in the Li1s spectrum, and 534 eV in the O1s spectrum (**Figure 5a** and **Figure S8c**). The enhancement of these peaks corresponding to carbonates ($ROCO_2Li$) may be attributed to the interaction between the Li anode and the methacrylate groups of the nanosheets, as a stable organic component in the SEI,[19] which also might help to protect the Li metal surface. In a comparison with the control sample, the content of Li_2CO_3, the thermodynamically unstable and brittle component in SEI, is much reduced in the FHMs as the extent of modification is increased (C1s in **Figure 5a** and **Figure S8c**), thus demonstrating that cells equipped with FHMs can form a more stable SEI layer to inhibit the electrolyte reduction and prevent side-reactions. LiF is considered to be an important component of the SEI layer for its strong mechanical strength and small surface diffusion barrier. It also enables uniform Li-ion flow to occur across both the bulk lithium and grain boundary regions of the SEI, due to the potential accumulative space charge effect in LiF combined heterostructure.[20] As depicted in the F1s and Li1s spectra shown in **Figure 5a**, the atomic ratio of the LiF component in FHM-D/A10 is much higher than that found in the other modified separators, which may due to a reduction of the electrolyte decomposition and fabrication of more stable LiF heterostructures via numerous functionalized nanosheets. This can also be supported by the relative intensity ratio of the LiF component in FHM-D/A5 (**Figure S8c**). The presence of more LiF on the surface of the Li anode could help to reduce the plane surface energy and Li nucleation overpotential (**Figure S6a**), which may promote further lithium nucleation and uniform growth. Besides, the wealth of LiF content in the SEI layer can serve to strengthen the SEI while suppressing lithium dendrite formation. Therefore, the presence of both $ROCO_2Li$ moieties and LiF involved in the interfacial layer are the main reason for the enhanced electrochemical stability of Li anode. To further investigate the influence of the nanosheets on the SEI, more attention will be devoted to the N1s spectra samples equipped with FHM-D/A10 and FHM-D/A5 (**Figure 5 and S8c-d**), which are the only sources of nitrogen. Evidently, three N1s peaks are observed on the Li anode-facing side of the SEI at 397.8, 400.2, and 402.6 eV and correspond to

C–N, amide/amine, and N^+, respectively[21-22]. The C–N and amide/amine groups stem from the intrinsic contents of the FHMs, while the N^+ component derives from the lithiation reaction of the NH groups with Li and the electrolyte.

Supporting Note 5. Cycle Performance in 1C, 2C and 4C rates of LFP|Li cells

The cycling performances of different LFP|Li full cells were firstly measured at constant current densities of 0.5C, 2C, and 4C, respectively, as shown in **Figure S12a,** and the charge-discharge curves of cells during repeated cycles are shown in **Figure S12 b-d**. Both the control cells showed sharp capacity fading and a low CE after 55 cycles at 0.5C. In contrast, the cells equipped with FHM separators exhibited a higher discharge capacity, an ultrahigh average CE (>99.2%), and a better capacity retention (97.4%) after 100 cycles (**Figure S12a**). The cell equipped with PP separator dropped abruptly from 131.2 to 98.9 mAh g^{-1} as the current rate increased to 2C, while in contrast the FHM cells exhibited almost no capacity fading upon cycling, respectively, implying that the as-prepared FHMs offered higher capacity retention and better cycling performance than the PP separator. Even at a 4C rate, the cell equipped with the FHM-D/A10 continued to achieve a high discharge specific capacity of 125.6 mAh g^{-1}, an average CE of 98.9%, and a corresponding retention ratio over 96.5% after 200 cycles (**Figure S12a**). These observations demonstrated that the FHMs can greatly enhance the cycling performance of LMBs. Furthermore, the charging/discharging profiles of the LFP|Li cells equipped with the FHM-D/A10 exhibited much lower voltage polarization than those equipped with the FHMs and PM, regardless of whether the cell was operated at 0.5C, 2C, or 4C, as depicted in **Figure S12b-d**. These results suggest that the LMBs equipped with the FHMs cycling performance, excellent interfacial stability, and potential dendritic inhibition compared with the control cells at different current densities.

Supporting Figures (S1-S15) and Tables (S1-S6)

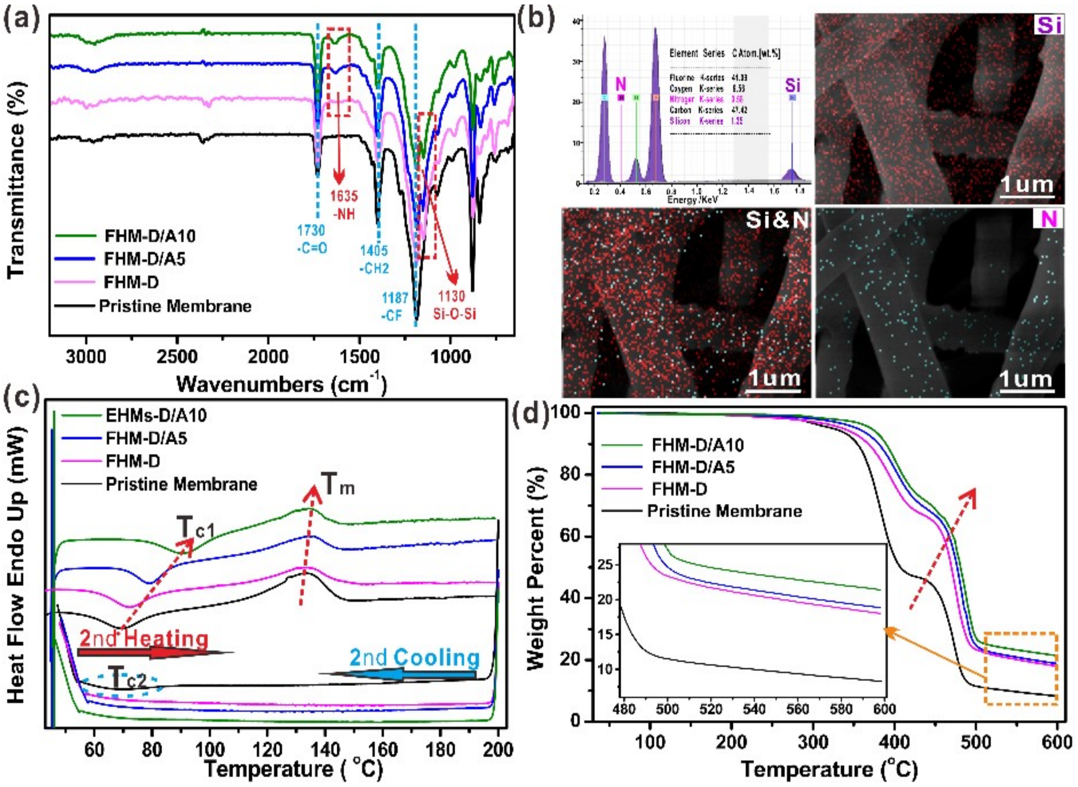

Figure S1. (a) FTIR curves of pristine polymer membranes, and FHMs with different addition of silsesquioxanes; (b) Typically energy-dispersive X-ray spectroscopic (EDX) profiles and the associated elemental maps for N and Si atoms on the surface of FHM-D/A10; (c) DSC characterization and (d) TGA profiles for PM and different FHMs.

Table S1. Summary of endothermic/exothermic peak and enthalpy results from the DSC performed twice scanning steps with heating-cooling-heating sequence. All enthalpy results have been normalized by deducting the mass portion of CSQs in membranes.

	Temperature / ^{o}C			ΔEnthalpy / J·g^{-1}		
	T_{c1}	T_{c2}	T_{m}	ΔH_{c1}	ΔH_{m}	ΔH_{c2}
Pristine Membrane	68.9	68.1	132.2	-9.28	8.91	-4.16
FHM-D	71.7		133.6	-10.03	11.52	
FHM-D/A5	79.2		134.7	-10.38	14.64	
FHM-D/A10	88.7		135.3	-11.70	15.01	

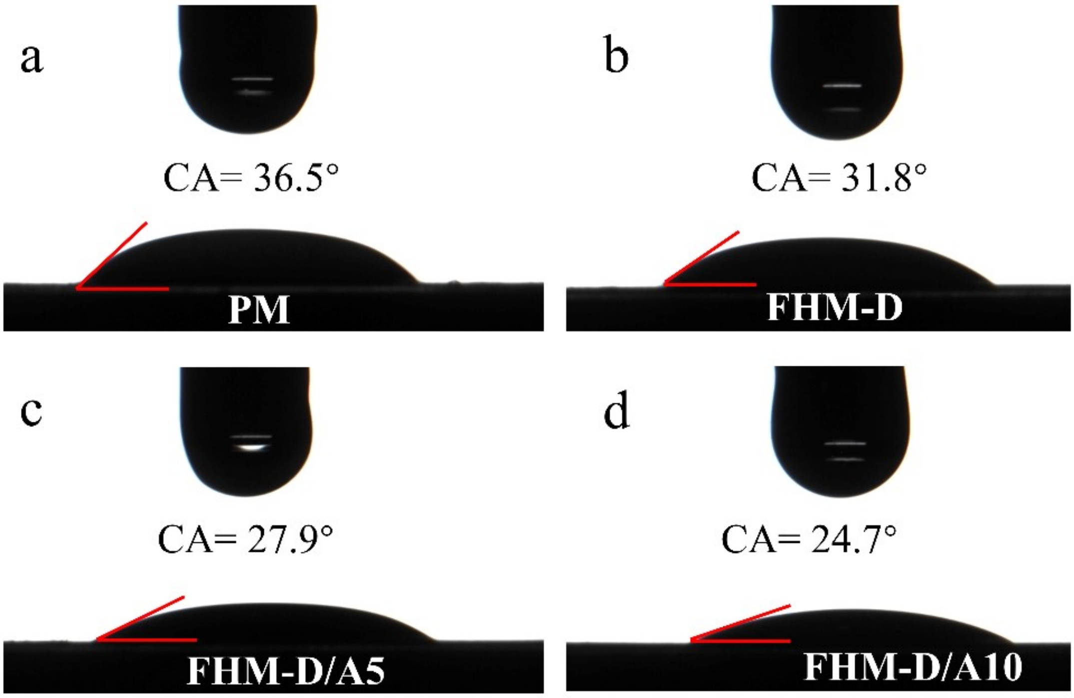

Figure S2. Contact angles of the ester electrolyte for (a) PM, (b) FHM-D, (c) FHM-D/A5, and (b) FHM-D/A10.

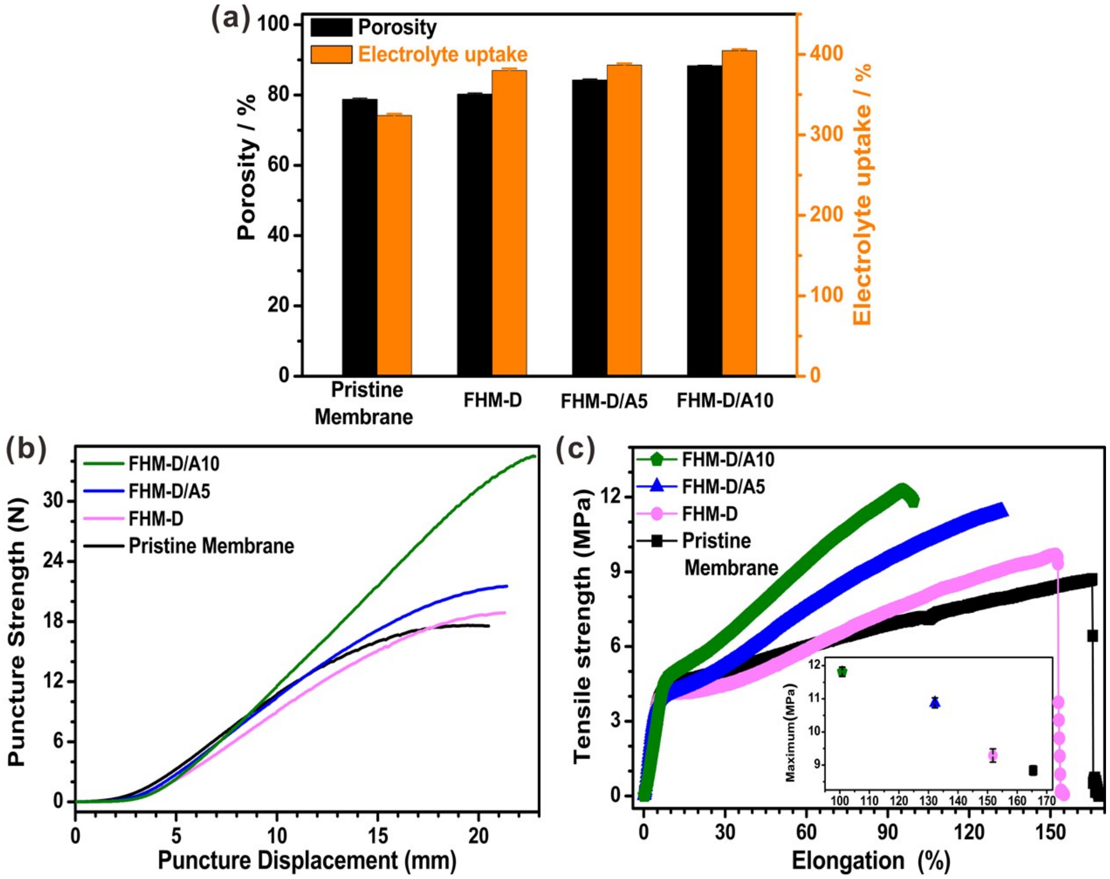

Figure S3. Basic porosity and mechanical properties of prepared membranes. (a) The results of porosity and electrolyte uptake, (b) displacement-strength curves for strength testing, and (c) strain-stress curves for tensile strength testing.

Table S2. BET surface areas, pore volumes, thickness, and EIS data of the pristine membrane and the FHMs fabricated with CSQ monomers and different ratios of OAPS.

	BET surface area [$m^2\ g^{-1}$]	Pore volume [$cm^3\ g^{-1}$]	Thickness [um]	R_b [Ω]	R_i [Ω]
Pristine Membrane	1.589	$1.76*10^{-3}$	$42^{\pm 5}$	4.25	175.3
FHM-D	1.902	$2.48*10^{-3}$	$49^{\pm 3}$	4.47	138.2
FHM-D/A5	2.132	$2.74*10^{-3}$	$46^{\pm 3}$	3.94	125.9
FHM-D/A10	2.824	$4.14*10^{-3}$	$45^{\pm 2}$	3.47	111.4

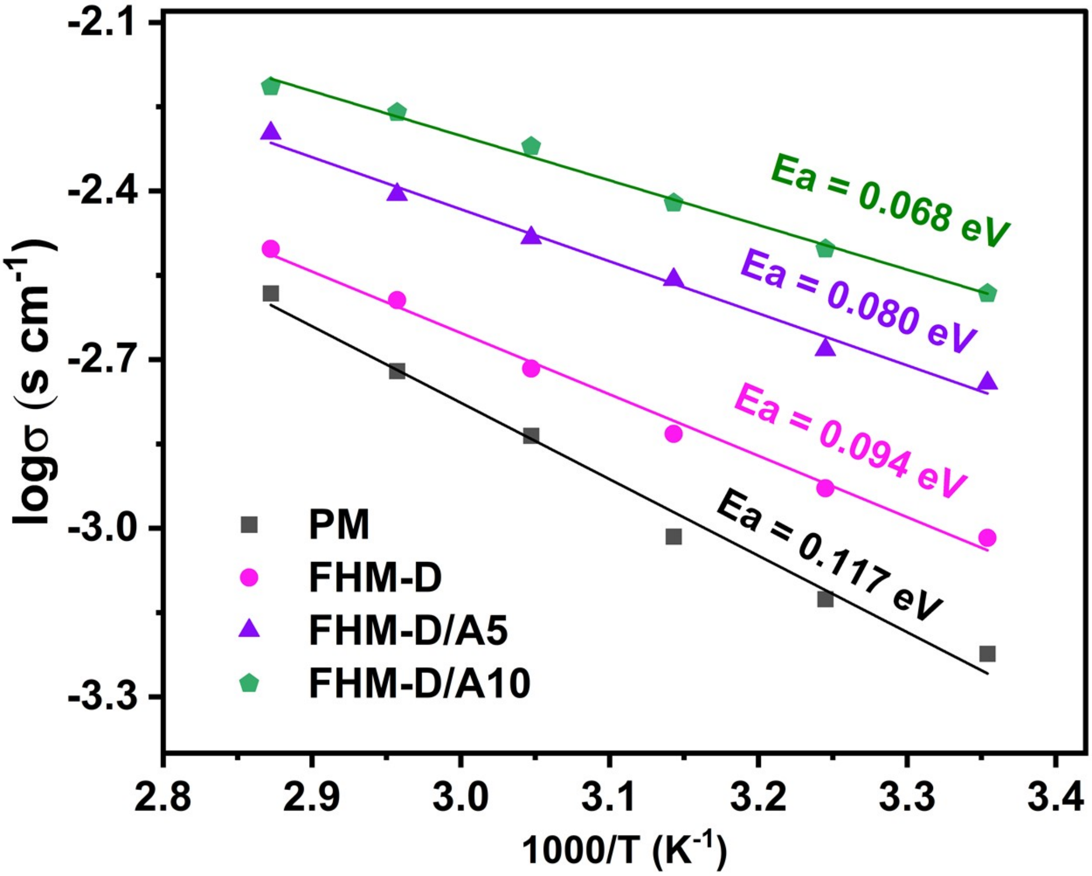

Figure S4. Ionic conductivity at various temperatures and activation energy gotten form linear fitting of the Arrhenius equation of PM and FHMs.

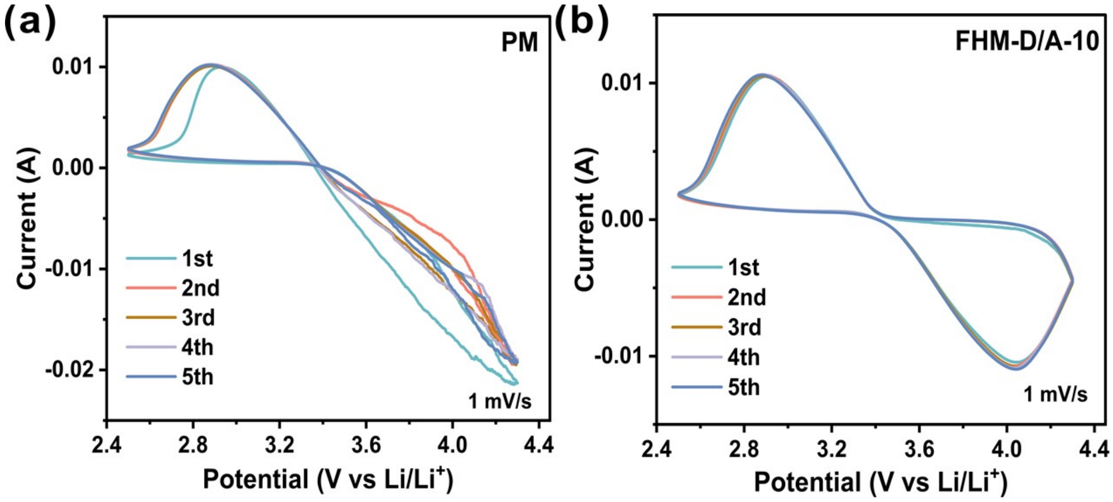

Figure S5. CV curves of Li||LFP cells with (a) PM and (b) FHM-D/A10.

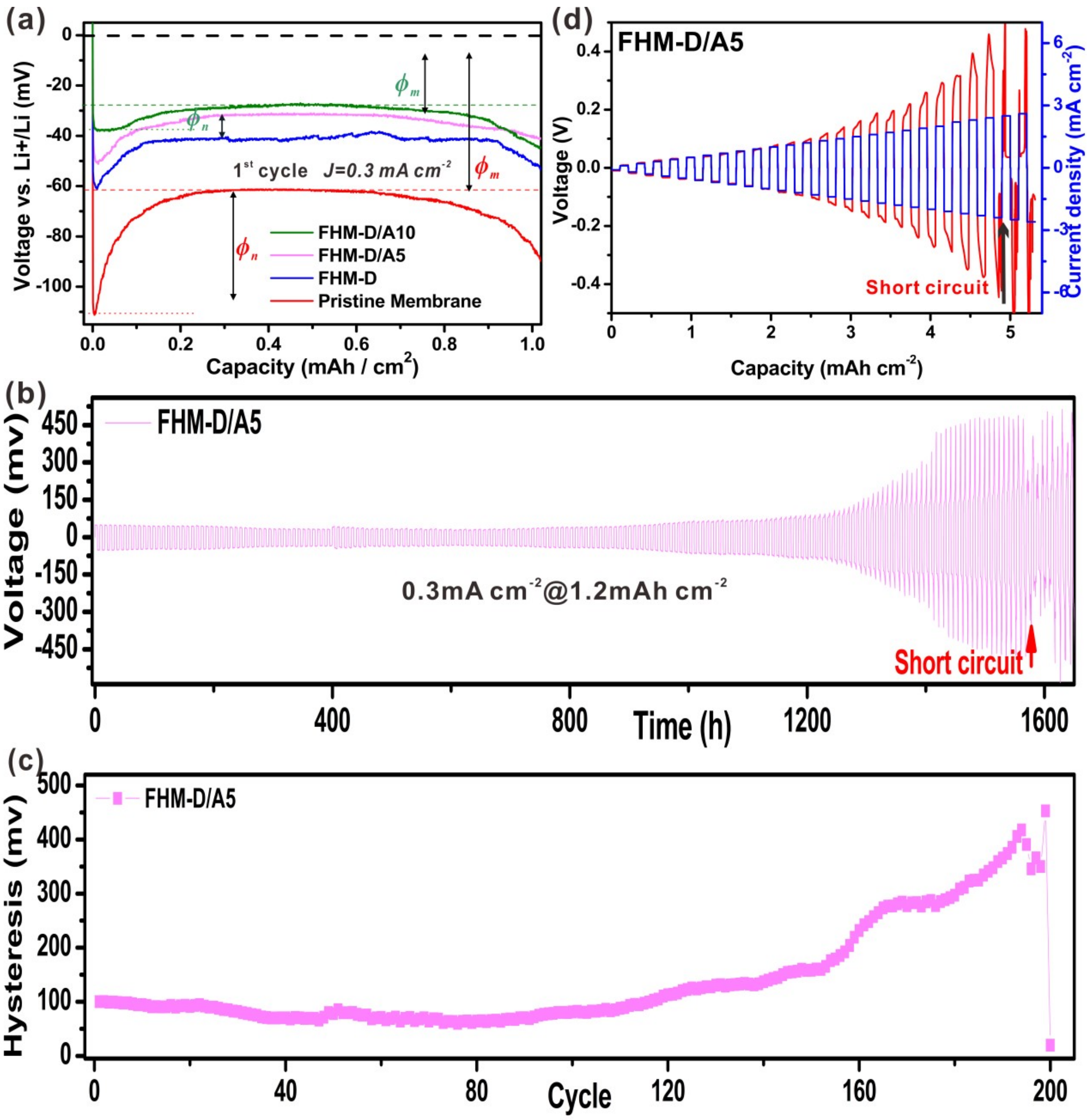

Figure S6. (a) Chronopotentiometry measurements at the initial cycle of the Li plating/stripping in the symmetric Li|Li cell with various separators. (b) The galvanostatic cycling profiles for Li|Li cell using the FHM-D/A5 with a current density of 0.3 mA cm^{-2} and a capacity of 1.2 mAh cm^{-2}. Insets show enlarged voltage profiles at a selected stage at a short time of different cells. (c) The hysteresis voltage of Li plating/stripping for cell with the FHM-D/A5. (d) Galvanostatic Li plating/stripping profiles in the Li|FHM-D/A5|Li cell (right) at step-increased current densities.

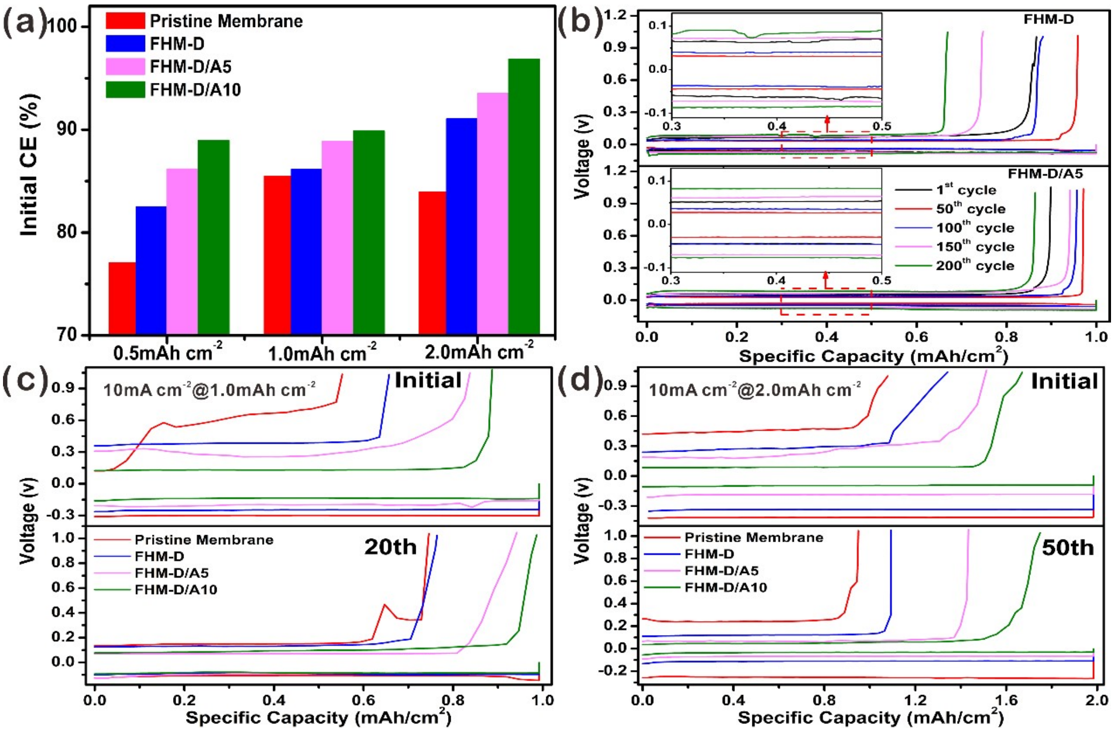

Figure S7. (a) Comparison of the initial coulombic efficiency of Li|Cu cells with pristine membrane and FHMs separators at 0.5 mA cm^{-2} with different capacity densities: 0.5(left), 1.0(middle), and 2.0(right) mAh cm^{-2}. (b) Voltage profiles of Li|Cu cells with FHM-D (top) and FHM-D/A5 (bottom) at different cycles, and a partially enlarged drawing of voltage hysteresis shown inset. Comparison of the CE Voltage profiles of Li|Cu cells with the PM and FHMs at the ultra-current density of 10 mA cm^{-2} with two capacity densities of (c) 1.0 and (d) 2.0 mAh cm^{-2}.

Table S3 Summary of cycling stability and Coulombic efficiency for asymmetric Cu/Li cells with different separators and electrolytes.

Materials	**Current density /mA cm^{-2}**	**Capacity /mAh cm^{-2}**	**Cycle number**	**Coulombic efficiency (%)**	**Electrolyte**	**Ref.**
LiMMT	1	1	300	99	1 M LiTFSI in DOL/DME with 1% LiNO$_3$	[23]

Adaptive “solid-liquid” protective layer	3	1	70	90	1 M LiTFSI in DOL/DME with 1% $LiNO_3$	[24]
3D glass fiber cloths (GF-modified Cu)	5	0.5	47	93	1 M LiTFSI in DOL/DME with 2% $LiNO_3$	[25]
	10	0.5	40	91		
PAN/AM-COF	2	2	80	99	1 M LiTFSI in DOL/DME with 1% $LiNO_3$	[26]
Oxidized Polyacrylonitrile and polyvinylpyrrolidone nanofiber	1	1	200	96	1 M LiTFSI in DOL/DME with 2% $LiNO_3$	[27]
	3	1	180	94.4		
	5	1	120	83		
3D carbon cloth supporting N-doped carbon nanosheet with Co (CC@CN-Co)	2	2	100	98.3	1 M LiTFSI in DOL/DME with 2% $LiNO_3$	[28]
3D-printed Cu framework (3DP-Cu)	1	5	45	95.5	1 M LiTFSI in DOL/DME with 1% $LiNO_3$	[29]
	5	5	65	91.9		
	10	5	100	＞90		
Functional hybrid membranes (**FHM-D/A10**)	1	1	150	93.8	1 M LiTFSI in DOL/DME with 1% $LiNO_3$	**Current work**
	5	1	150	84.2		
	10	1	60	87.0		
	10	2	60	91.2		

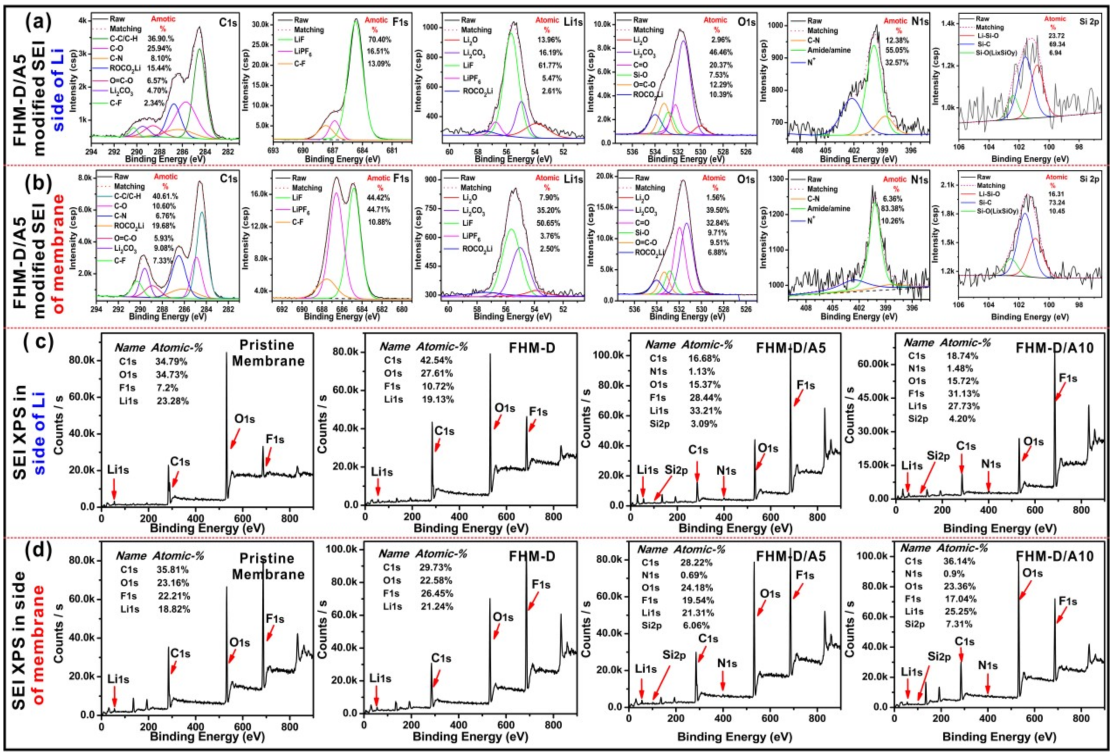

Figure S8. XPS analysis and the relevant atomic ratio of elements for the various separator in the surface of (a) the anode side and (b) the separator side. The components in the SEI layer for the LFP |Li battery with the FHM-D/A5 after cycled at 10 C rate for 200 cycles. The signals from the surface of the anode side and the separator side are shown in (c) and (d), respectively.

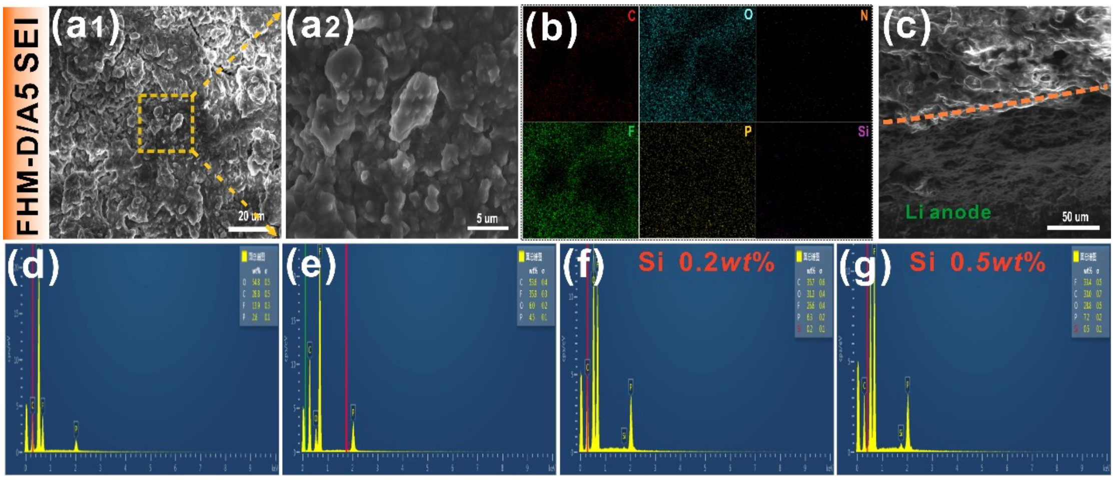

Figure S9. (a1-2) The top-view FE-SEM images and partially enlarged drawings, corresponding EDS mapping for a2 of the elements with C, N, O, F, Si, and P are shown in the mapping, and (c) the cross-section FE-SEM images of the Li anode harvested from the LFP|Li cells with FHM-D/A5, respectively. (d-g) EDS data analysis of element for Li anodes from the LFP|Li cells assembled by the PM, FHM-D, FHM-D/A5, and FHM-D/A10, respectively. All LFP|Li cells were operated at 10 C rate after 200 cycles in a fully discharged state.

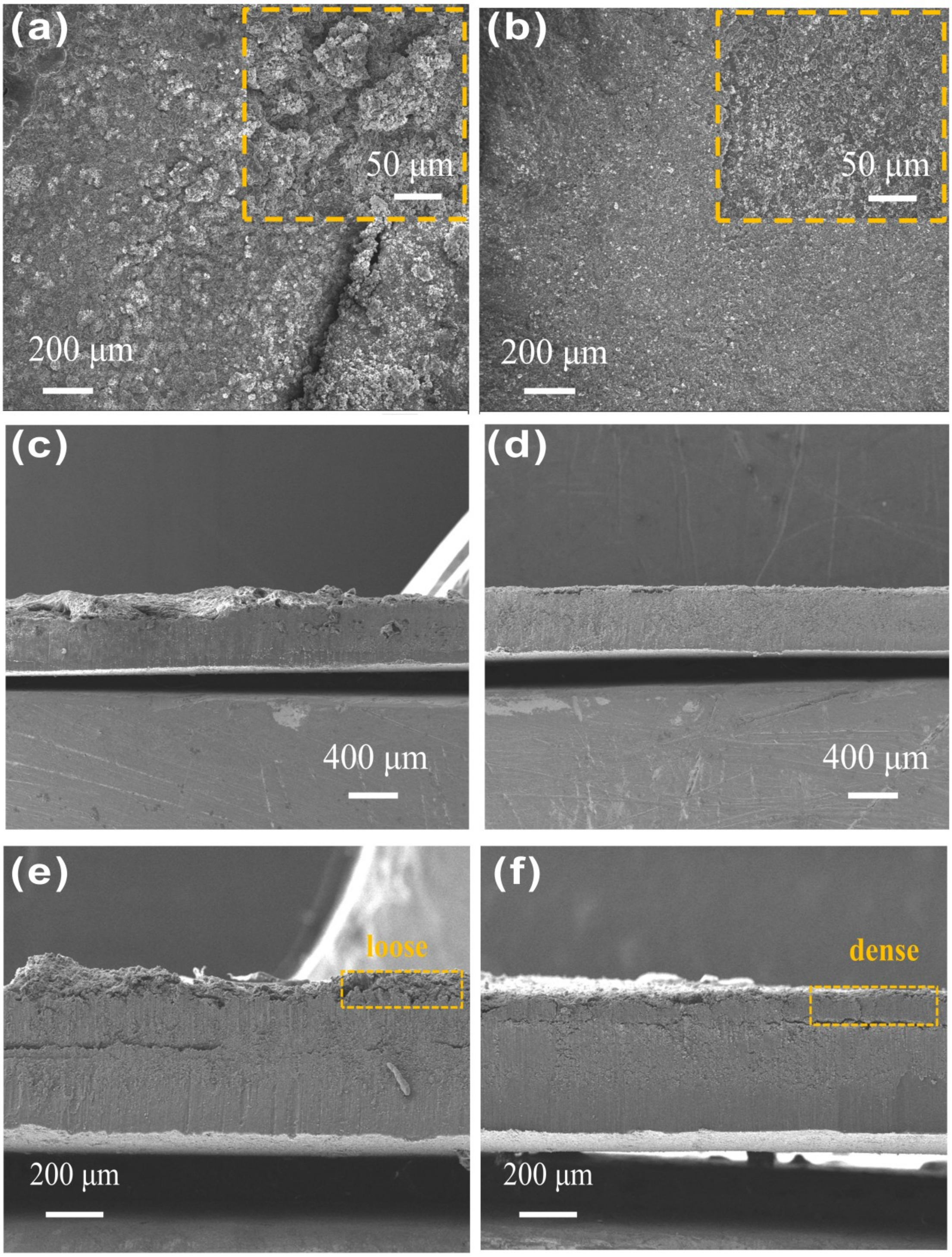

Figure S10. (a) Top view and (c) cross-section view of SEM images of cycled lithium metal disassembled from Li/PM/LFP cell. (b)Top view and (d) cross-section view of SEM images of cycled lithium metal disassembled from Li/FHM-D/A10/LFP cell.Cross-section view of SEM images of cycled lithium metal disassembled from Li/LFP cell with (e) PM and (f) FHM-D/A10 separators.

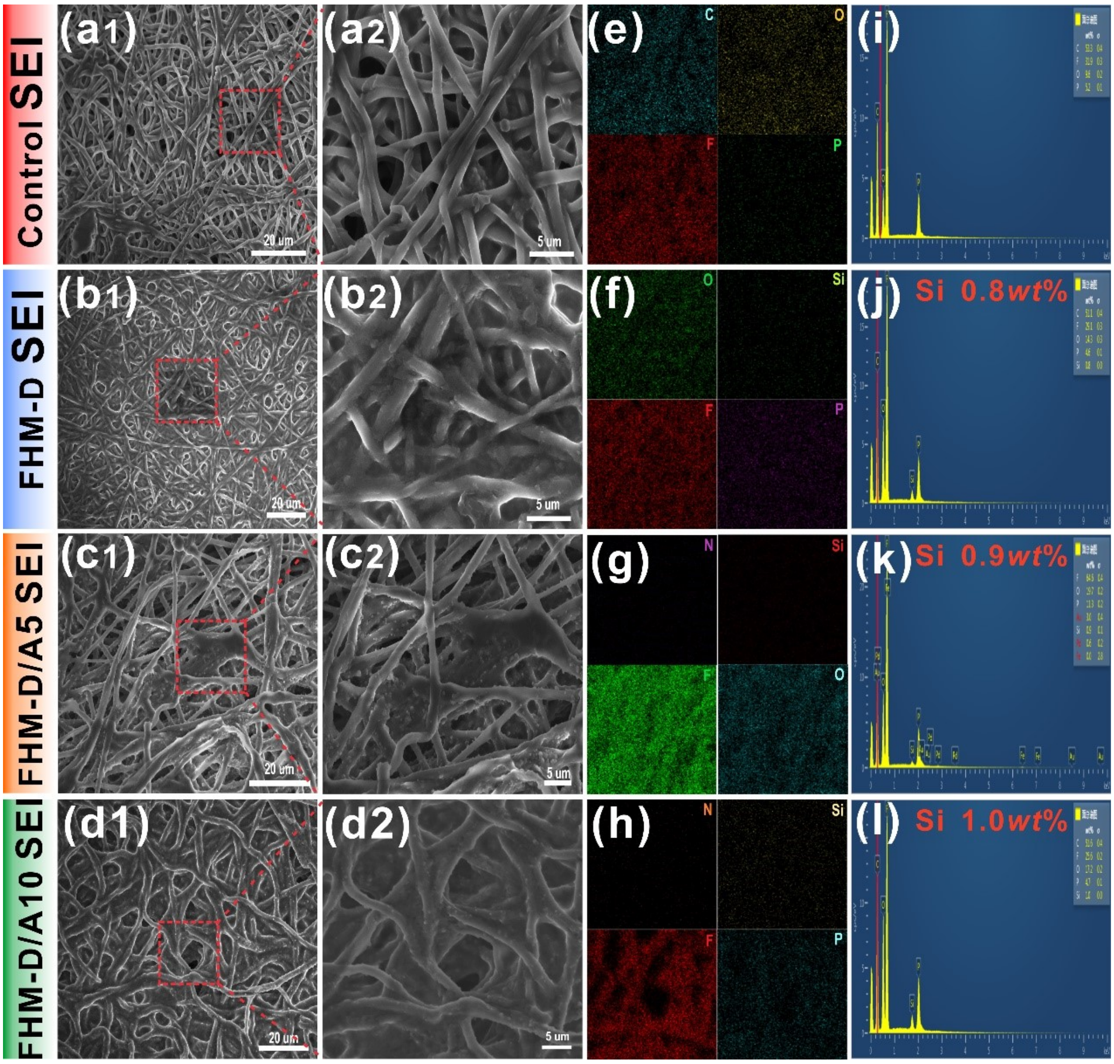

Figure S11. (a-d) The top-view FE-SEM images and partially enlarged drawings, (e-h) corresponding EDS mapping for a2-d2 of the elements with C, N, O, F, Si, and P are shown in the mapping, and (i-l) EDS data analysis of element for the separator (near Li side) from the LFP|Li cells assembled by the PM, FHM-D, FHM-D/A5, and FHM-D/A10, respectively. All LFP|Li cells were operated at a 10 C rate after 200 cycles in the fully discharged state.

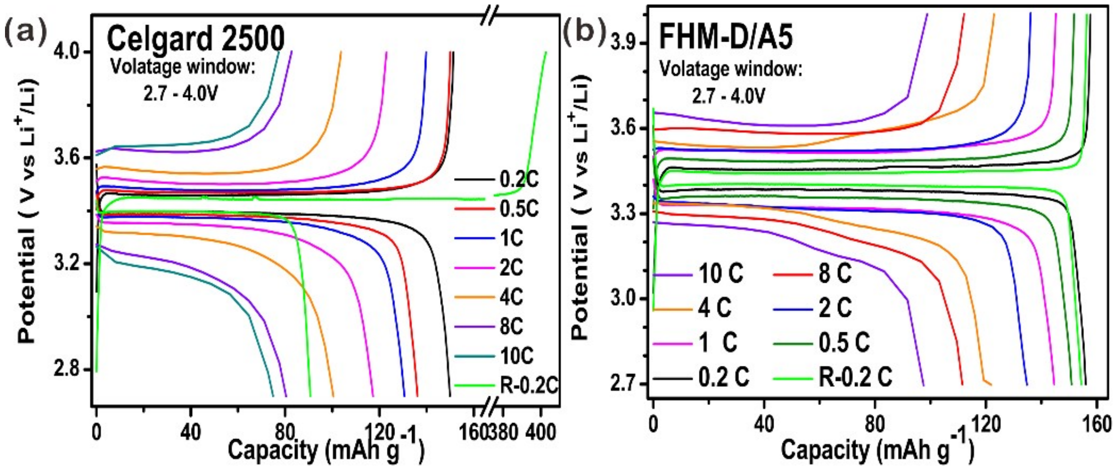

Figure S12. The galvanostatic charge/discharge profiles of cells with (a) the PP separator and (b) the FHM-D/A5 at different current rates.

Table S4. The comparison of overpotentials in different charge/discharge current rates of the LFP/Li cells assembled by various separators.

Separators	**Overpotentials in different current rates** (mV)							
	0.2C	0.5C	1C	2C	4C	8C	10C	R-0.2C
Celgard 2500	68.5	122.4	170.1	193.7	237.2	455.1	581.9	60.8
Pristine Membrane	49.3	83	104.2	154.1	256.1	432.8	481.7	45
FHM-D	40.3	72.6	93.6	147.3	207.1	350.3	413.9	40
FHM-D/A5	41.8	62	74.3	137.7	198.3	304.1	369	39.4
FHM-D/A10	39.7	50.6	66	110	159.7	224.1	266	36

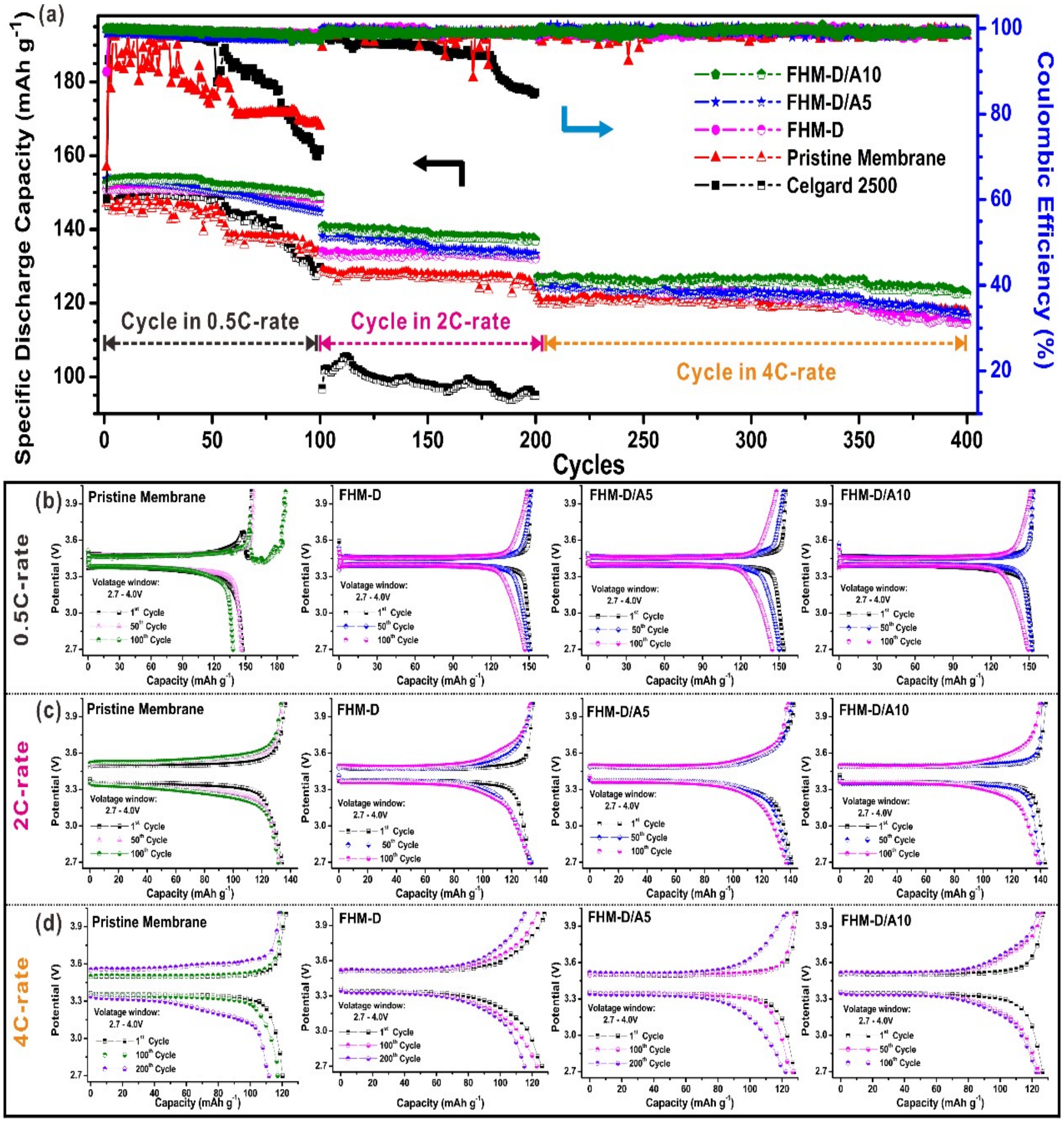

Figure S13. Cycle performance of LiFePO$_4$ /Li cells assembled by PP separator, PM, and the FHMs. (a) The cycling performance at the current rates of 0.5 C, 2 C, and 4 C in different cycles; the comparison of galvanostatic charge/discharge profiles for the cell with the pristine membrane and the FHMs separators in the 1st, 100th, and 200th cycle at (b) 0.5 C, (c) 2 C, and (d) high 4 C rate.

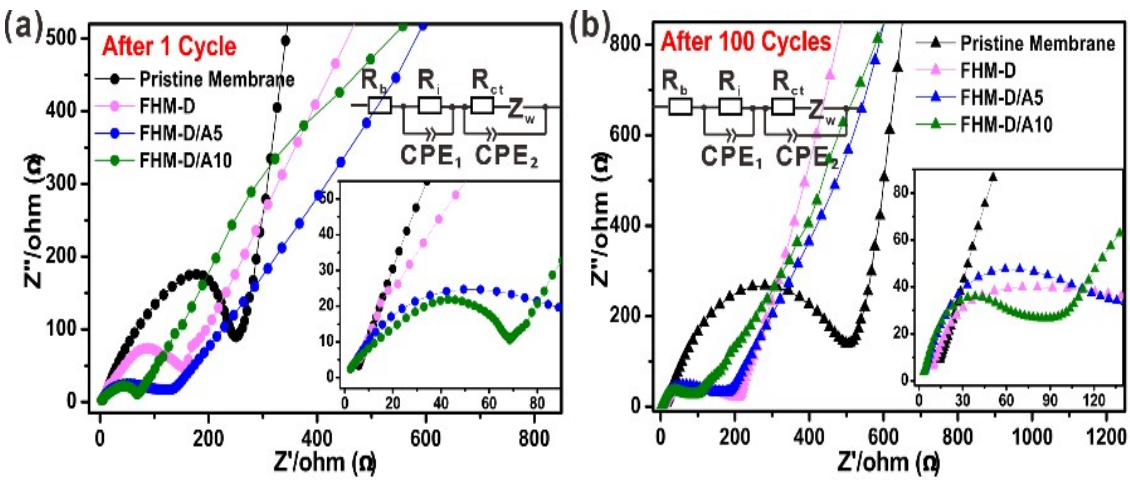

Figure S14. Experimental EIS curves of the LFP/Li cell with as-prepared separators after (a) 1 cycle and (b) 100 cycles at 2 C current rate, measured after completely discharge state.

Table S5. Simulation results of **Figure S14**.

	1st Cycle			**100th Cycle**		
	R_b	**R_i**	**R_{ct}**	**R_b**	**R_i**	**R_{ct}**
Pristine Membrane	5.83	177.67	244.74	14.53	280.37	490.03
FHM-D	4.47	88.50	153.05	8.98	120.71	206.31
FHM-D/A5	2.84	49.38	119.63	3.97	59.21	162.59
FHM-D/A10	2.26	32.91	66.32	3.25	38.56	83.90

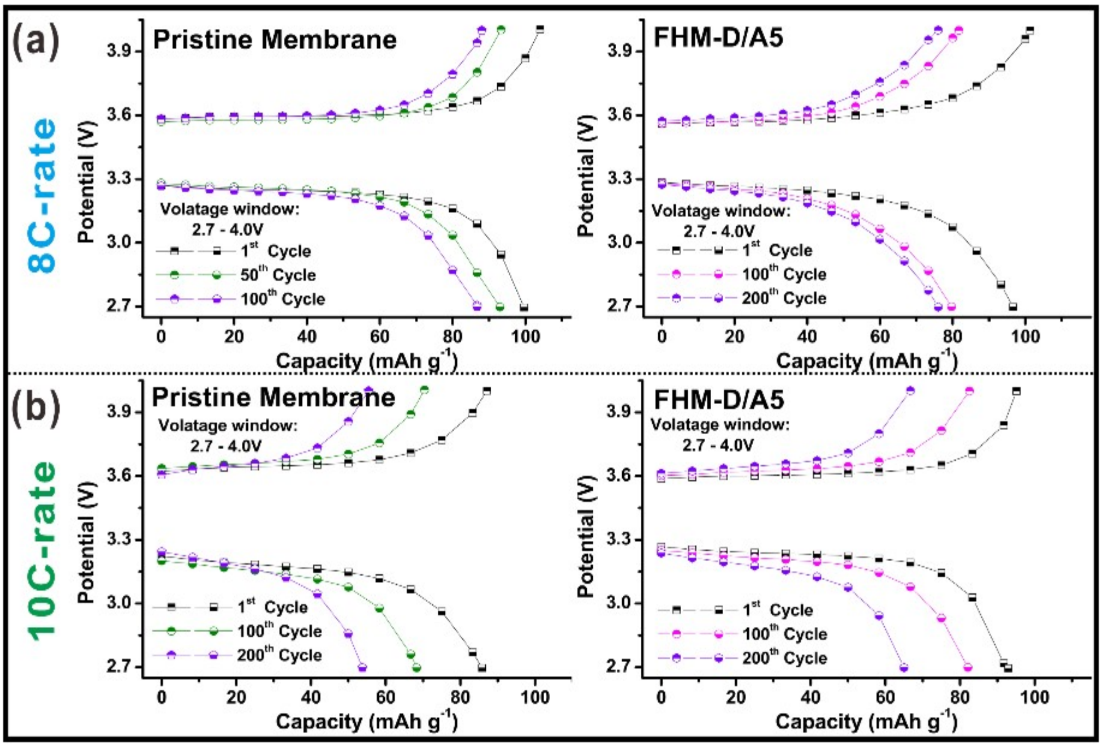

Figure S15. The comparison of galvanostatic charge/discharge profiles for the cell with the pristine membrane and the FHM-D/A5 separator in the 1st, 100th, and 200th cycle at (a) 8 C and (b) ultrahigh 10 C rate.

Figure S16. The dQ/dV curves of the Li||LFP cells with (a) PM and (b) FHM-D/A10 cycled at ultra-high 10C.

Table S6 Summary of cycling performance and Coulombic efficiency at high rates for the LFP/Li cells with different separators, anodes, and electrolytes.

Materials (separator)	**Current rate /C**	**Capacity retention /%**	**Cycle number**	**Coulombic efficiency /%**	**Electrolyte**	**Ref.**
LFP || Li (PE-PEG-CPE)	3	89.1	350	93	1M $LiPF_6$ in EC/DMC/EMC(1:1:1)	[30]
LFP || Li (PVDF-HFP/SN)	2	86	50	67	1M $LiPF_6$ in EC/DEC(1:1)	[31]
LFP || Li (PVDF-HFP/garlic separator)	10	87.5	100	91	1M LiPF6 in EC/DEC/DMC/EMC(30:15:20:35)	[32]
LFP || Li (Artificial SEI PSf/MoO_3 fiber celgard 2400)	2	80	500	96	1M $LiPF_6$ in EC/DEC(1:1)	[33]
LFP || Li (Sandwich-structured CGC separator)	3	76.44	146	86	1M $LiPF_6$ in EC/DEC(1:1)	[34]
LFP || Li (Functional hybrid membranes **FHM-D/A10**)	2	97.4	100	99.2	1M $LiPF_6$ in EC/DMC/EMC(1:1:1)	**Current work**
	4	96.2	200	98.9		
	8	91.3	200	98		
	10	92.04	100	97.5		

Supporting References

[1] J. Peng, K. Xu, H. Cai, J. Wu, W. Lin, Z. Yu, M. Chen, *RSC Advances* **2014**, 4.

[2] a) Brown J F, Vogt L H, Prescott P I. *Journal of the American Chemical Society* **1964**, 86(6): 1120-1125.; b) Brown Jr, John F. *Journal of the American Chemical Society* **1965**, 87.19: 4317-4324.

[3] Abraham, K. M., Jiang, Z., & Carroll, B. Highly conductive PEO-like polymer electrolytes. *Chemistry of Materials* **1997**, 9(9), 1978-1988.

[4] S. Grimme, C. Bannwarth, P. Shushkov. A Robust and Accurate Tight-Binding Quantum Chemical Method for Structures, Vibrational Frequencies, and Noncovalent Interactions of Large Molecular Systems Parametrized for All spd-Block Elements (Z = 1−86). *J. Chem. Theory Comput.* **2017**, 13.

[5] C. Bannwarth, S. Ehlert, S. Grimme. GFN2-xTB—An Accurate and Broadly Parametrized Self-Consistent Tight-Binding Quantum Chemical Method with Multipole Electrostatics and Density-Dependent Dispersion Contributions. *J. Chem. Theory Comput.***2019**, 15, 1652-1671.

[6] A. J. C. S. Part. Toward reliable density functional methods without adjustable parameters: The PBE0 model. *Journal of chenical physics.* **2000**, 110.

[7] F. Weigend, R. Ahlrichs. Balanced basis sets of split valence, triple zeta valence and quadruple zeta valence quality for H to Rn: Design and assessment of accuracy. *PCCP*. **2005**, 3297-3305.

[8] X. Li, W. Chen, Q. Qian, H. Huang, Y. Chen, Z. Wang, Q. Chen, J. Yang, J. Li, Y. W. Mai. Electrospinning-Based Strategies for Battery Materials. *Adv. Energy Mater*. **2020**, 11.

[9] Electrospinning of nanofibres. *Nature Reviews Methods Primers*. **2024**,4, 2.

[10] Z. Tu, Y. Kambe, Y. Lu, L. A. Archer, *Advanced Energy Materials* **2014**, *4*.

[11] D. Aurbach, A. Zaban, A. Schechter, Y. Ein-Eli, E. Zinigrad, B. Markovsky, *Journal of The Electrochemical Society* **2019**, *142*, 2873-2882.

[12] Abraham K M, Jiang Z, Carroll B. *Chemistry of materials* **1997**, 9(9): 1978-1988.

[13] D. Dong, H. Zhang, B. Zhou, Y. Sun, H. Zhang, M. Cao, J. Li, H. Zhou, H. Qian, Z. Lin, H. Chen, *Chem Commun (Camb)* **2019**, *55*, 1458-1461.

[14] M. J. Baran, M. E. Carrington, S. Sahu, A. Baskin, J. Song, M. A. Baird, K. S. Han, K. T. Mueller, S. J. Teat, S. M. Meckler, C. Fu, D. Prendergast, B. A. Helms, *Nature* **2021**, *592*, 225-231.

[15] X. Peng, K. Huang, S. Song, F. Wu, Y. Xiang, X. Zhang, *ChemElectroChem* **2020**, *7*, 2389-2394.

[16] M. S. Kim, J.-H. Ryu, Deepika, Y. R. Lim, I. W. Nah, K.-R. Lee, L. A. Archer, W. Il Cho, *Nature Energy* **2018**, *3*, 889-898.

[17] Q. Zhao, R. Zhou, C. Wang, J. Kang, Q. Zhang, J. Liu, Y. Jin, H. Wang, Z.

Zheng, L. Guo, *Advanced Functional Materials* **2022**, 32, 2112711.

[18] Y. Qian, K. Chen, Z. Feng, Y. Ouyang, Q. Lan, C. Zhang, W. Feng, Y.-E. Miao, T. Liu, *Small Structures* **2023**, 4, 2200383.

[19] P. Bhattacharya, M. I. Nandasiri, D. Lv, A. M. Schwarz, J. T. Darsell, W. A. Henderson, D. A. Tomalia, J. Liu, J.-G. Zhang, J. Xiao, *Nano Energy* **2016**, *19*, 176-186.

[20] Y. Sun, Y. Zhao, J. Wang, J. Liang, C. Wang, Q. Sun, X. Lin, K. R. Adair, J. Luo, D. Wang, R. Li, M. Cai, T. K. Sham, X. Sun, *Adv Mater* **2019**, *31*, e1806541.

[21] Y. Ji, B. Yuan, J. Zhang, Z. Liu, S. Zhong, J. Liu, Y. Liu, M. Yang, C. Wang, C. Yang, J. Han, W. He, *Energy & Environmental Materials* **2022**, 7.

[22] Meng, J., Chu, F., Hu, J., & Li, C. *Advanced Functional Materials* **2019**, 29(30), 1902220.

[23] Zhang, Z., Wang, J., Qin, H., Zhang, B., Lin, H., Zheng, W., Ou, X. *ACS nano* **2024**, 18(3), 2250-2260.

[24] L. Zuo, Q. Ma, P. Xiao, Q. Guo, W. Xie, D. Lu, X. Yun, C. Zheng, Y. Chen, *Advanced Materials* **2023**, 36, 2311529.

[25] Wang, X., Wen, Y., Wang, Y., Chen, Y., Yang, L., Guo, C., Xie, X. *Journal of Power Sources* **2024**, 615, 235126.

[26] Wang, K., Duan, J., Chen, X., Wang, J., Li, J., Jiang, L., Liao, Y. *Advanced Energy Materials* **2024**, 2401146.

[27] S. Zhou, Y. Zhang, S. Chai, I. Usman, Y. Qiao, S. Luo, X. Xie, J. Chen, S. Liang, A. Pan, H. Zhou, *Chemical Engineering Journal* **2021**, 404.

[28] T. Zhou, J. Shen, Z. Wang, J. Liu, R. Hu, L. Ouyang, Y. Feng, H. Liu, Y. Yu, M. Zhu, *Advanced Functional Materials* **2020**, 30.

[29] G. J. H. Lim, Z. Lyu, X. Zhang, J. J. Koh, Y. Zhang, C. He, S. Adams, J. Wang, J. Ding, *Journal of Materials Chemistry A* **2020**, 8, 9058.

[30] Li, Y., Yang, J., Zhang, X., Cui, X., Pan, Q. *Journal of Materials Chemistry A* **2023**, 11(16), 9029-9038.

[31] Y. Ji, L. Dong, J. Liu, H. Xie, S. Zhong, C. Yang, J. Han, W. He, *Energy & Environmental Science* **2024**, 17, 4078-4089.

[32] B. Boateng, Y. Han, C. Zhen, G. Zeng, N. Chen, D. Chen, C. Feng, J. Han, J. Xiong, X. Duan, W. He, *Nano Lett* **2020**, 20, 2594.

[33] C. Dong, Z. Lin, Y. Yin, Y. Qiao, W. Wang, Q. Wu, C. Yang, D. Rooney, C. Fan, K. Sun, *Journal of Energy Chemistry* **2021**, 55, 1.

[34] R. Pan, R. Sun, Z. Wang, J. Lindh, K. Edström, M. Strømme, L. Nyholm, *Nano Energy* **2019**, 55, 316.